Desalination and Water Treatment
www.deswater.com

doi: 10.5004/dwt.2021.26644

209 (2021) 402–413
January

Characteristics of Er-doped zinc oxide layer: application in synthetic dye solution color removal

Hajer Chemingui[a,b,*], Jalila Chékir Mzali[a], Takwa Missaoui[a], Mehmet Konyar[c], Moez Smiri[a,d], H. Cengiz Yatmaz[e], Amor Hafiane[a,*]

[a]*Laboratory of Water, Membrane and Environmental Biotechnology, CERTE, BP 273, Soliman 8020, Tunisia, emails: hajerchemingui2@gmail.com (H. Chemingui), amor.hafiane@certe.rnrt.tn (A. Hafiane)*
[b]*Faculty of Sciences of Tunis, University of Tunis El Manar, 2092 El Manar, Tunisia*
[c]*Chemistry Engineering Department, Istanbul Technical University, Istanbul, Turkey*
[d]*College of Sciences and Arts Sager Campus Boys, Shaqra University, Shaqraa, Riyadh, Saudi Arabia*
[e]*Environmental Engineering Department, Gebze Technical University, Gebze, Kocaeli, Turkey*

Received 19 November 2019; Accepted 7 October 2020

ABSTRACT

The objectives of this work were carried out to exhibit a simple, cost-effective, non-toxic, and solid-state reaction route to prepare ZnO nanoparticles (NPs) of rare earth erbium. Material characterizations using X-ray diffraction (XRD), FTIR, UV-Visible, photoluminescence (PL) and scanning electron microscopy methods were performed. The FTIR spectrum indicates the presence in the prepared products of both. The objectives of this work were to demonstrate a simple, cost-effective, non-toxic, and solid-state reaction route for the preparation of ZnO zinc oxide and erbium oxide. The XRD patterns suggest that the ZnO NPs are crystalline and that the Er ions have been incorporated into the ZnO lattice position. It was also noted that different Er concentrations have a powerful effect on ZnO NP morphology, band breakthrough, PL and photocatalytic function. Doped ZnO samples showed significant increase in photodegradation of RR180 azo dye molecules under UV light irradiation for 45 min. Photocatalytic research has shown that the degradation rate has risen to 3 wt.%, with the rise in the Er concentration. This research obviously demonstrates that the doping of erbium's ZnO could be an opportunity to enhance its photocatalytic efficiency.

Keywords: Er-doped ZnO nanoparticles; Solid-state reaction; Optical properties; Photocatalytic activity; SEM

1. Introduction

Dyes are one of the textile sector's most significant contaminants and a few of their major contaminants in the climate [1]. Both human and marine life are sensitive to the presence of these pollutants in ground and surface water. Some of them are carcinogenic, mutagenic, genotoxic and water-cleaning technology is required [2]. Various physical and chemical procedures were employed for the removal of color from textile effluents such as precipitation, adsorption by activating carbon, coagulation and membrane separation [3,4].

Hence, it is important to develop new treatments, which are more efficacious in the damage of dyes from wastewater. The use of advanced oxidation processes has been found to be an appropriate way of degrading various organic pollutants such as organic aqueous dyes. The photocatalytic process can be considered to become the most effective way to reduce water contamination, potentially destroying a wide variety of organic molecules and harmless compounds [5,6]. Photocatalysis that used a semiconductor (ZnO, TiO_2, SnO_2) under UV light causes electrons to change from valence band to conduction band [7,8]. The electron-hole pairs formulated could very well interact with O_2 and H_2O molecules to form superoxide

* Corresponding author.

anions ($O_2^{\bullet-}$) and ($^{\bullet}OH$) radicals, which have more oxidizing and reducing properties for dye compounds used in several industries [8,9].

ZnO is one of the semiconductor materials used for photocatalytic degradation process due to its huge availability, non-toxicity and chemical stability. It has a wide band-gap (3.3 eV) and a free exciton binding energy of 60 eV at room temperature with a variety of interesting electronic and optical properties [10–12]. Currently, many studies on this material are being carried out by several researchers [13,14]. Many methods were used to prepare ZnO such as chemical vapor deposition [15], thermal evaporation [16], sol-gel method [17], co-precipitation process [18] and solid-state reaction method. Among these techniques, the solid-state reaction method is the most used due to some characteristics: low cost, easy adjusting composition and doping elements, simplicity and rapidity.

Doping zinc oxide improves its performance such as photocatalytic activity, conductivities, etc. [19–21]. Among many dopants, rare-earth doped ZnO nanomaterials have potential applications in many technologies such as degradation of pollutants and optoelectronic devices [22,23]. The trivalent rare earth (RE) ions enhance optical properties of ZnO due to its partially filled 4f energy level, surrounded by full 5s and 5p orbitals. The rare earth ions are better luminescent materials because of the sharp and intense emission due to their 4f intra-shell transitions [24,25]. Among the RE ions, the Er^{3+} (erbium) has attracted significant attention due to its enormous potential in various applications [26]. Many researchers have reported the formation of Er-doped ZnO nanostructures and reported their unique and distinct properties and applications [1,27]. Zamiri et al. [28] have observed that the Er dopant has a strong effect on the structure and photoluminescence (PL) characteristics of ZnO nanorods.

To the best of our knowledge, very few studies have been published on the comparison of photocatalytic degradation of organic pollutants by the ZnO nanostructures doped with RE metal. The enhancement of the photocatalytic activity of ZnO nanoparticles (NPs) and the photosensitivity toward UV light irradiation using doping agents have, therefore, attracted more consideration [29]. Sin et al. [30] and Khataee et al. [31] reported the photocatalytic activity of ZnO:Er^{3+} nanomaterials synthesized using sonochemical methods. In both cases, the photocatalytic degradation rate was significantly lower than the pure ZnO nanostructures.

The objectives of this study are (i) to prepare Er-doped ZnO NPs via a low-cost method, (ii) to investigate the effect of different Er doping concentrations on various properties of ZnO NPs and (iii) to evaluate the photocatalytic activity of the Er-doped ZnO NPs using Remazol Red Brilliant F3B (RR180) as a model textile of azo dye.

2. Materials and methods

2.1. Materials

Nano powder ZnO (99.99% purity, CAS: 1314-13-2) and Er_2O_3 (99.99% purity) were purchased from Sigma-Aldrich (USA). NaOH (98% purity) and ethanol (99% purity) were obtained from Merck (Tunisia). Remazol Brilliant Red F3B (Reactive Red 180) (RR180), used as model dye for photocatalysis experiments, was supplied by Dystar (Turkey) and used without further purification.

2.2. Synthesis of photocatalyst

Er^{3+}-doped ZnO powder samples have been prepared via a controlled solid-state reaction route at a high temperature according to the literature [32]. A percentage of Er^{3+} (from 1% to 5%) was mixed with ZnO powder in the presence of NaOH pellets that operate as a heat supplier. The mixture was carefully homogenized after measuring the specific substance in the proportions calculated to obtain 5 g of powder. The slurry obtained was then dried in the oven at 100°C. The powder was rigorously ground for 2 h using a mortar and then poured into an aluminum crucible to be heated to 700°C for 5 h. The final powder was ground for 15 min and used for characterization and catalysis experiments.

2.3. Characterizations

X-ray diffraction (XRD) was performed using a Philips X-ray diffractometer with Cu-Kα radiation (λ = 0.15406 nm). The crystalline structure of the samples was analyzed by using (PANanalytical X'PERT PRO model X-ray diffractometer, CNRSM, Tunisia), at a voltage of 50 kV and a current of 30 mA. The morphology, size distribution and energy-dispersive X-ray spectrum (EDS) were determined using scanning electron microscopy (SEM; Philips XL30 SFEG, Turkey). Fourier-transform infrared spectra were recorded under identical conditions in the 400–4,000 cm^{-1} region using Fourier-transform infrared spectrometer (SHIMADZU). The UV-Vis spectra were carried out using the Lambda-35 (PerkinElmer, Tunisia) spectrophotometer in the wavelength range of 200–800 nm. Photoluminescence (PL) emission spectra were recorded using a fluorescence spectrophotometer (Agilent, Tunisia). The samples were excited with a 325 and 488 nm wavelength light at room temperature.

2.4. Photocatalytic degradation process

A fresh 500 mL aqueous RR180 azo-dye solution was produced throughout every photocatalytic degradation cycle in order to accomplish a 50 mg/L concentration by preparing the solution for the dye. Degradation reactions were performed in a laboratory-scale photoreactor capable of housing UVA emitting wavelength lamps. The details of the design of the reactor were provided elsewhere by Kocakuşakoğlu et al. [33]. The lamp intensity measured by the UV light meter was 3.18 mW/cm^2 for UVA (Lutron UVA-365, Turkey). In order to feed and speed up reactions and maintain reactor temperature about 25°C, cooled air was blown into the batch reactor. During the reactions, the solution's temperature and pH were controlled. In order to examine the synthesized powder behavior, the concentration of catalyst ZnO was changed to 0.5 g/L. The suspension in an ultrasonic bath was sonicated for 30 min and maintains the powder distribution uniform. Samples were taken from the solution

in 15 min during the experiments to detect concentration change. At a centrifugation rate of 6,000 rpm, each sample was centrifuged, which then detected the absorption by a 540 nm UV-Vis spectrophotometer (DR3800 Hach, Turkey). With the Beer–Lambert law, the absorbance data are translated to the concentration values. The following formula measured the finished color removal rate (% R) values:

$$\%R = \frac{(C_0 - C)}{C_0} \times 1 \quad (1)$$

where C_0 is the concentration of RR180 at equilibrium established under dark conditions and C is the concentration of the dye solution taken at irradiation time interval t (from 10 to 90 min).

3. Results and discussion

3.1. X-ray diffraction analysis

XRD patterns of ZnO:Er^{3+}, with different concentrations of Er^{3+}, collected over a 2θ range of 20°–80° are plotted in Fig. 1. Diffraction peaks correspond to the reflections from planes (100), (002), (101), (102), (110), (103), (200), (112), (201), (004) and (202) of wurtzite ZnO structure, which is consistent with the standard (JCPDS 89-0510). The high diffraction peaks at 2θ (degree) of 31.8°, 34.5° and 36.2° were indexed as (100), (002) and (101) planes, respectively. The intensity of peaks reflected the high degree of crystallinity of the NPs and they indicate the formation of the pure hexagonal phase of wurtzite ZnO.

It was observed that peaks in the XRD pattern at 2θ = 29.4°, 48.9° and 58.02° are characteristic planes for pristine Er_2O_3 (JCPDS 077-0777). We noticed also that the concentration of erbium was increased further extra phase related to Er_2O_3. The peak corresponding to (222) plane of Er_2O_3 arises at 29.43° and is observed in Fig. 1 (3% Er–5% Er).

Table 1 shows the calculated crystallite size of ZnO:Er^{3+} NPs. The crystallite size was determined by means of the X-ray line broadening method using the Debye–Scherrer equation [34,35]:

$$D = \frac{0,9 \times \lambda}{\beta \cos\theta} \quad (2)$$

where λ is the wavelength of the X-ray (λ = 1.54 Å for CuKα), β is the broadening of the diffraction line measured at half of its maximum intensity (FWHM: full width at a half maximum), θ is the Bragg's diffraction angle and D is the crystallite size.

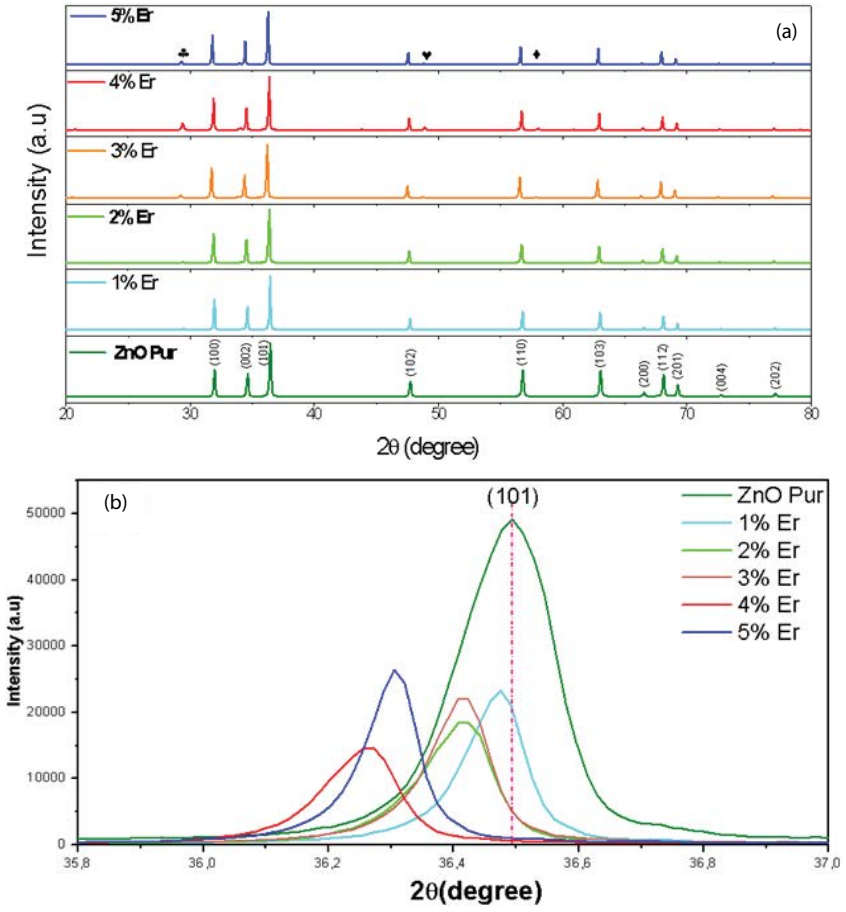

Fig. 1. XRD patterns of Er-doped ZnO Nps with different concentrations (a) and evolution of the preferred orientation peak (1 0 1) (b).

As Er doping content rose from 1 to 5 wt.%, the position of the (101) peak was slightly shifted toward the lower angles (Table 1), indicating the substitution of Er in the ZnO lattice (Fig. 1b). As shown, the weakness of their full width at half maximum may indicate an improvement of the crystallinity of ZnO. Moreover, the broadening of the diffraction peaks and the weakness of their intensity with increasing of Er content, constitute an indication that Er doping inhibited the growth of crystal grain. Thus, the peak is shifted towards the lower angle side. Moreover, John and Rajakumari [36] show that the return of peak to the parent position related to the excess amount of erbium atoms starting to increase the strain in the lattice. Indeed, Rita and Rajaram demonstrate that the peaks in the diffraction pattern of doped samples are slightly shifted as compared with undoped ZnO. This shows that small variations in the lattice parameters occur as the Er^{3+} concentration increases. The nanocrystals exhibited changes in relative intensities and crystallite size with changes in the doping concentration of erbium [35], which is in accordance with our results. By comparison with other works of ZnO doped with other rare-earth ions, we found that our results are concordant with them [36–39]. The increase in the lattice parameter and the shift to the lower angle of the XRD peaks (Table 1) affected the deformation and strain lattice [40].

The lattice strain is calculated through the following formula:

$$\varepsilon = \frac{\beta}{4\tan\theta} \tag{3}$$

As seen in Table 1, the lattice strain of ZnO:Er^{3+} decreases with the decrease of % Er^{3+} till 3 at %, then it increases. For the concentrations higher than 3 at %, the excess of Er^{3+} ions leads to the formation of Er–O–Zn on the ZnO surface which may inhibit the growth of the crystal grain and causes stress from the outside to the inside of the crystal. Besides, from Table 1, at lower doping concentration, the volume of the unit cell, as well as cation–anion bond length, is decreasing. This is due to the replacement of Zn^{2+} ions with Er^{3+} ions in the crystal lattice. Nevertheless, as the concentration of doping increases, the lattice parameters also are increased due to the interstitial incorporation of erbium ions in the ZnO matrix. After a literature survey, we found that the decrease in the crystal size of ZnO-doped Eu^{3+}/Dy^{3+} was mainly attributed to the formation of Eu(Dy)–O–Zn on the surface of the doped products, which inhibited the growth of crystal grains [41–43].

3.2. FTIR spectroscopy

To further confirm the chemical composition of synthesized nanostructures, FTIR spectroscopy was done in the range of 400–4,000 cm^{-1}. The FTIR spectra of (ZnO–Er) NPs are shown in Fig. 2a. It can be seen that all absorption bands observed in spectra are characteristic of ZnO Nps. Indeed, broadband appeared in the region 3,550–3,100 cm^{-1} indicating a plentiful presence of hydroxyl groups [16,44] (O–H stretching vibration).

In addition, the absorption bands observed at 1,610 and 1,780 cm^{-1} are probably due to the O–H of water molecule [45]. The intense bands observed at 1,420 cm^{-1} are linked to the absorption of CO_2 from the air by the catalyst [43]. The broadband situated at 506 cm^{-1} is due to transverse optical stretching modes of ZnO. The vibrations of Er–O are located at 569 and 550 cm^{-1}. These results are compared with the literature [46] and our data. It is worth pointing that the FTIR spectra of ZnO–Er (different %) Nps showed only one broad peak at ~550 cm^{-1}, because the peak arising from Zn–O and Er–O are in the same wavelength region near (540–490 cm^{-1}).

FTIR peaks have functional groups displayed in Table 2. These results indicate that both zinc and erbium are present as oxides in the material (Fig. 2b).

3.3. Scanning electron microscopy

To examine the elemental composition of the prepared NPs, EDS attached with FESEM was used. Fig. 3 presents the SEM images of pure and rare-earth doped ZnO:*x* wt.% Er samples (*x* = 0%, 1%, 2%, 3%, 4% and 5%). Different morphologies can be observed depending on the percentage of the dopant ion incorporated. The absence of extra peaks, besides the expectable ones in nanocrystals, suggests that the obtained products are very pure. As shown in the images, the samples exhibit "nanoparticle" features with serious aggregation. Interestingly, the shapes for all the Er-doped ZnO NPs are almost the same and are in the range of 195–75 nm. It was also observed that the size of the NPs decreases with an increase in the Er-doping concentration. It is observed that, as the erbium doping concentration increases up to 3 wt.%, the size of the particles

Table 1
2θ value of the preferred orientation of (101), the corresponding *a* and *c* parameters (Å), c/a, FWHM value, cell volume and strain (ε) of undoped and Er-doped ZnO

ZnO:Er (at %)	*a* (Å)	*c* (Å)	*c/a*	Cell volume (Å^3)	2θ (°)	(FWHM) (rad)	*D* (nm)	Strain (ε)
0	3.243	5.193	1.603	47.22	36.410	0.0037	95.47	0.0028
1	3.244	5.197	1.602	47.36	36.474	0.0021	87.54	0.0015
2	3.245	5.194	1.600	47.26	36.270	0.0017	75.91	0.0012
3	3.248	5.202	1.601	47.12	36.639	0.0014	60.78	0.0010
4	3.247	5.204	1.602	47.54	36.306	0.0015	101.50	0.0011
5	3.241	5.201	1.604	47.48	36.344	0.0016	104.21	0.0012

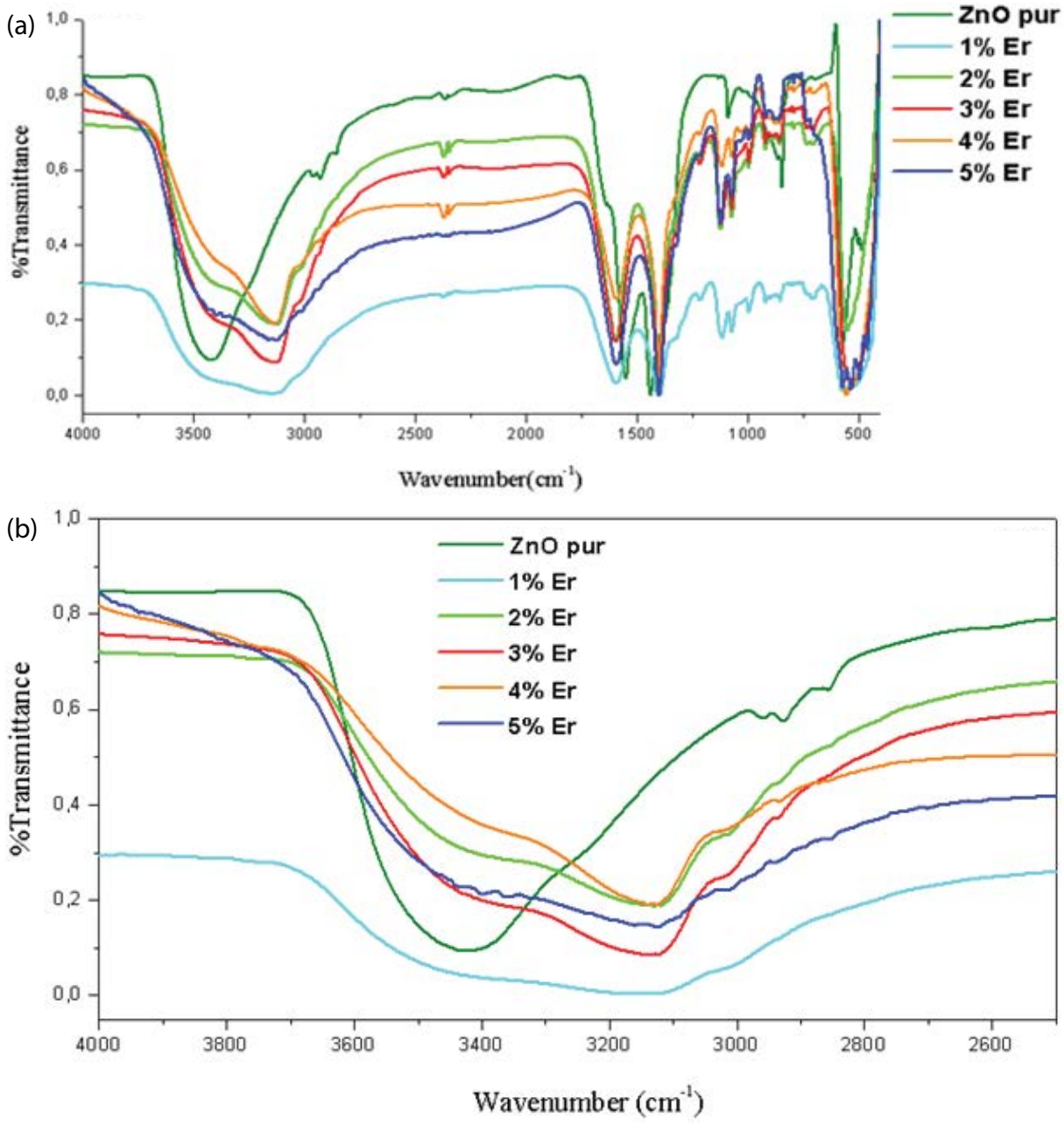

Fig. 2. (a) FTIR absorption spectra of ZnO-doped Er at different concentrations. (b) Zoom of the 400–650 cm^{-1} range of the FTIR spectra of Er-doped ZnO nanoparticles.

Table 2
Functional group present in the synthesis of Er-doped ZnO NPs analyzed by FTIR

Absorption peak (cm^{-1}) in Er-doped ZnO NPs	Bond/functional groups
3,550–3,100 cm^{-1}	O–H stretching vibration
1,610 cm^{-1}	O–H of water molecule
1,420 cm^{-1}	CO_2 groups
569 and 550 cm^{-1}	Er–O stretching vibration
506 cm^{-1}	Zn–O elongation vibration

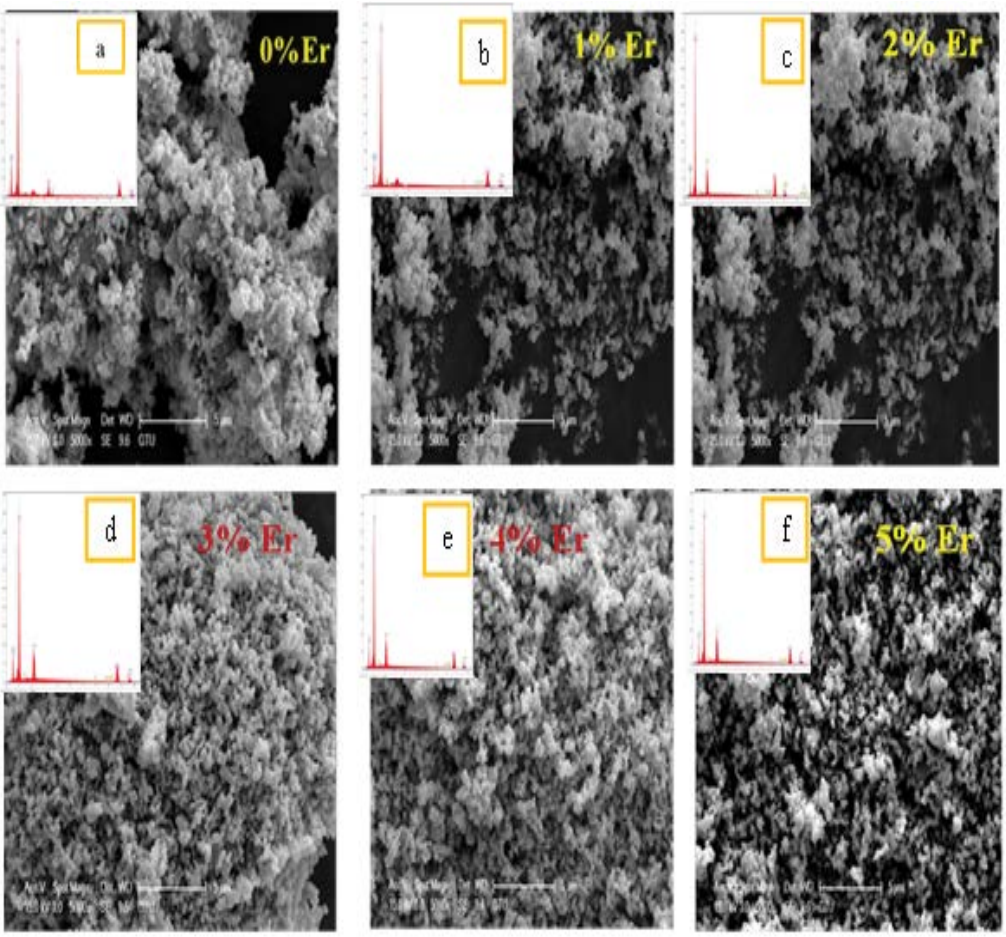

Fig. 3. SEM images and EDS spectrum of samples (a) pure ZnO, (b) 1 wt.% Er-doped ZnO, (c) 2 wt.% Er-doped ZnO, (d) 3 wt.% Er-doped ZnO, (e) 4 wt.% Er-doped ZnO and (f) 5 wt.% Er-doped ZnO.

gets decreased and while the concentration again increased, the size starts to increase but still in the nanometer range up to 5 wt.%. Minimum particle size is observed for 3 wt.% erbium-doped sample. This is due to the effect of doping on the nucleation mechanism in the growth process. Since the ionic radius of Er^{3+} is larger than that of Zn^{2+} ions, are strained nucleation rate and a consequent lower growth rate of the samples will appear.

Insets of Figs. 3a–f represent the typical EDS along with elemental compositions of Er-doped ZnO NPs for EZ-1 to EZ-6 samples. It is noted that 1% Er-doped ZnO NPs sample (EZ-2) does not have any Er peak, which may be due to the presence of very low concentration of Er ion. However, all other samples showed well-defined peaks for Er ions. Further, except Zn, O and Er, no other peak related to any impurity was seen in the spectrum, up to the detection limit of EDS, which confirmed that the prepared NPs are Er-doped ZnO without any significant impurity.

3.4. Optical properties

3.4.1. UV absorption

The optical properties of pure ZnO, 1%, 2%, 3%, 4%, and 5% Er-doped ZnO were investigated, by UV-visible as shown in Fig. 4. No other peaks presented in the spectrum, which confirms that the as-synthesized product was pure ZnO. By comparison, to the bulk ZnO, the 3% Er-doped ZnO shows an absorption peak at 380 nm. This redshift can be explained by the formation of a shallow level inside the bandgap due to impurity atoms residing in the lattice. It is worth to point that ZnO absorption is sensitive to Er content. In addition, the spectrum relative to ZnO:Er (1%) indicates the presence of weak absorption bands related to the f–f transitions from the $^4I_{15/2}$ ground state to the $^4F_{5/2}$, $^4F_{7/2}$, $^2H_{11/2}$ and $^4S_{3/2}$ levels.

The Er-doped ZnO NPs exhibited a notable absorption band edge shift towards the long wavelength region, which demonstrates a decrease of the bandgap energy. The bandgap energy (E_g) of semi-conductor material was calculated by using the following equation [47]:

$$E_g = \frac{1,240}{\lambda} \tag{4}$$

The approximated direct band gap energy of the ZnO, 1 wt.%, up to 5 wt.% Er is 3.32, 3.29, 3.28, 3.26, 3.25 and 3.23 eV, respectively, as shown in Table 3. Zhang et al. [48] and Faraz et al. [49] described similar results.

Table 3
Maximum absorption value λ_{max} (nm) and E_g (eV) value of undoped and Er-doped ZnO

Echantillon	ZnO pure	1% Er	2% Er	3% Er	4% Er	5% Er
λ_{max} (nm)	373	376	379	376	378	383
E_g (eV)	3.32	3.29	3.27	3.29	3.28	3.23

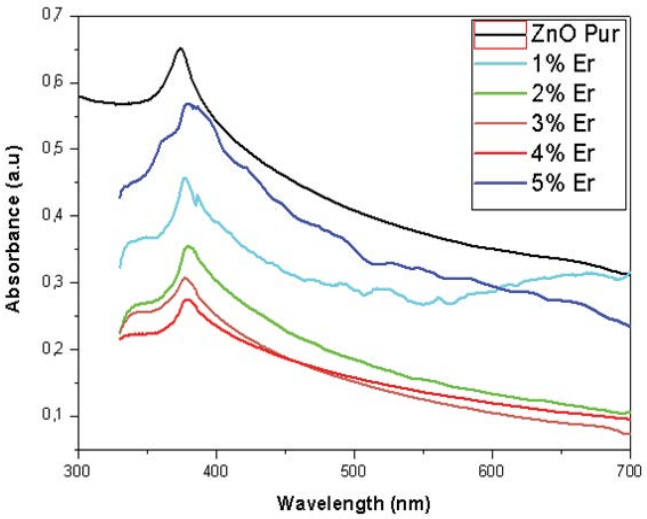

Fig. 4. Absorption spectra of ZnO Nps (% Er) recorded at room temperature in the UV-Vis range.

The bandgap values of the photocatalyst diminished in the range of 3.32 – 3.23 eV as doping of Er dose increases, which is shown in Fig. 4. The change in band gap values with the increasing doping concentration may be due to the introduction of the doping levels in ZnO lattice, which would induce the excitation of an electron from the valence band to the conduction band [50]. The wavelength range of 3 wt.% Er-doped ZnO catalyst was red-shifted of about 60 nm and absorption intensity increases [51].

First, it is clear that the E_g value increases with Er doping from 3.29 eV for ZnO (1%) to 3.26 eV for the optimum concentration 3 at.%. Guesmi et al. [37] gave an advanced explanation. In this research, pure ZnO and 3% Dy-doped ZnO have the optical energy band gaps of 3.03 and 2.89 eV, respectively. Energy gap (E_g) of pure ZnO is slightly lower than that of 3.2 eV for intrinsic bulk ZnO [27,39].

3.4.2. Photoluminescence characterization

Figs. 5 and 6 exhibit the photoluminescence excitation spectra of the ZnO-doped erbium registered by monitoring the excitations at 325 and 488 nm, respectively. The spectra of all products consist of similar bands characterizing the Er^{3+} ions.

From Fig. 5, it exhibited six excitation bands at 378, 435, 465, 486, 518 and 544 nm which correspond to the different transitions of $^4G_{11/2}\rightarrow{}^4I_{15/2}$, $^4F_{3/2}\rightarrow{}^4I_{15/2}$, $^4F_{5/2}\rightarrow{}^4I_{15/2}$, $^4F_{7/2}\rightarrow{}^4I_{15/2}$, $^2H_{11/2}\rightarrow{}^4I_{15/2}$, and $^4S_{3/2}\rightarrow{}^4I_{15/2}$, respectively. The appearing bands at around 568 nm are attributed to the $^2F_{9/2}\rightarrow{}^6H_{13/2}$ transition of the dysprosium ion Dy^{3+}. Indeed, even if all the starting

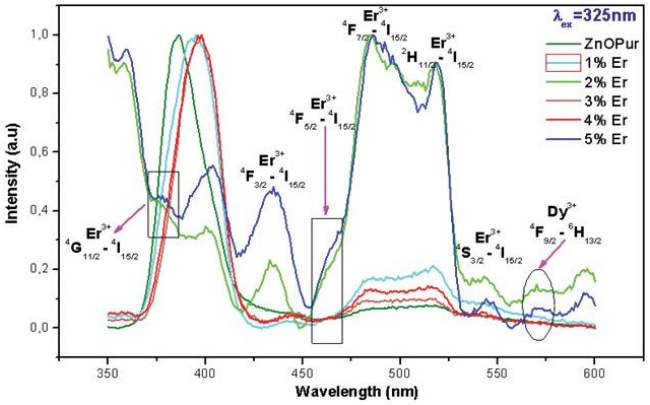

Fig. 5. Emission spectra of ZnO (% Er) recorded at 325 nm wavelength recorded at room temperature.

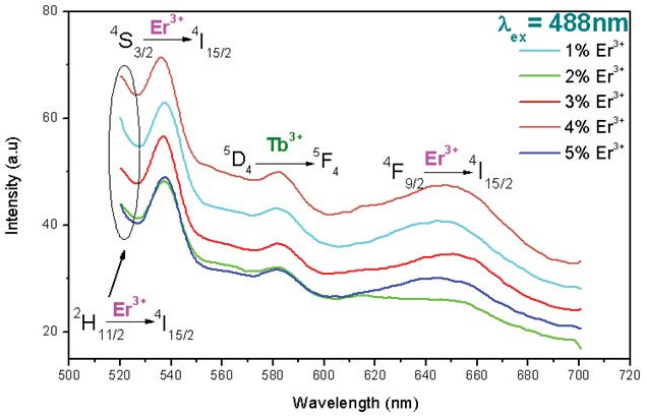

Fig. 6. Emission spectra of ZnO:Er at different concentrations, recorded at 488 nm wavelength at room temperature.

materials used have purity (99.9%), we cannot avoid the presence of rare earth impurities such as terbium "Dy^{3+}" [51]. Anyway, it seems that the parasitic emission appears clearly even at both low and high concentrations (Fig. 5). In addition, Jagannatha Reddy et al. [52] indicate explicitly in their works that the impurities doped into semiconductors will lead to more vacancies.

The broadening of the UV-violet band after Er doping can be explained by the overlapping between the exciton PL band and the violet PL band, centered at 407 nm. This is linked to the creation of Zn vacancies and Zn interstitials defects from Er doping. On the other hand, it was observed that the intensity of the band of ZnO is reduced after doping up to 2% Er^{3+}. This can be related to possible excitation transfer from intrinsic defects to Er^{3+}. However, an enhanced

intensity that has been recorded of the visible bands is seen after doping with Er^{3+}. As shown, the PL intensity of the four emissions of Er^{3+} increases with increasing Er^{3+} ion, reaching a maximum value of 2% and then a quenching is observed. According to the literature, the quenching effect can arise from different processes:

- Based on works of Jlassi et al. [67], for concentrations above 2%, high interactions between Er^{3+} ions lead to an increase of the non-radiative process originated from PL quenching.
- According to Ajimsha et al. [68], the origin of an extinction phenomenon may be due to the process of cross-relaxation, in the close Er^{3+}–Er^{3+} pairs. In fact, it can occur when the distance between the two ions is reduced.

Interestingly, it is observed that the intensity of green emissions has considerably increased for all Er-doped ZnO studied compounds suggesting the increase in oxygen vacancy defects.

Fig. 6 represents room temperature photoluminescence spectra of Er^{3+}-doped ZnO at an excitation wavelength of 488 nm, recorded in the visible range. All spectra show the characteristic emission bands of Er^{3+}resulting from the intra-configurational electronic from different excitation levels to $^4I_{15/2}$ fundamental level. Such features are usually related to the crystallized environment of the rare-earth ions. In fact, four main emission bands are identified (Fig. 6). It is well established that the main routes to improve photocatalytic activity is the efficient electron–hole (exciton) recombination.

In regard to the strongest and large band is located around 386 nm is undoubtedly originated from the recombination of the free excitons in ZnO [53,54]. Therefore, our results are in good accord with the literature [52]. In addition, it is worth to point that the broad band located from 421 to 600 nm is not only connected to erbium ions but also related to the Zn vacancy (VZn) [55], intrinsic defects such as O-vacancy (VO)[56], Zn-interstitial (Zni)[57], O interstitial (O_i) and extrinsic impurities [58]. Usually, the presence of the oxygen vacancies (V_O) and zinc interstitial (Zn_i) in the ZnO matrix is confirmed by the green emission [59–61]. Furthermore, it is known that the oxygen vacancies can occur in three different charge states: the singly ionized oxygen vacancy (V_O*), the doubly ionized oxygen vacancy (V_O**) and the neutral oxygen vacancy (V_O^0). Among them, only (V_O*) can act as luminescent centers (green emission) in the ZnO matrix. Therefore, the green emission results from the recombination of a photogenerated hole with the single ionized charge state of the defect [62,63]. Anyway, and by comparison with recent reports, it seems that the deep-level-defect luminescent centers of V_O* and Zn_i are both the main origins of the green emission. Similar results are reported in the literature [64–66]. Therefore, Erbium causes the enhancement in electron–hole recombination and thus leads to an improvement in the photocatalytic performance of the Er-doped ZnO.

3.5. Photocatalytic activity analysis

To illustrate their impact on environment application in the elimination of contaminants from wastewater, the photocatalytic behavior of undoped and Er-doped ZnO NPs has been studied for the photodegradation of RR180 aqueous solution under UV light irradiation.

The photodegradation of Remazol Red Brilliant F3B on the surface of Er-doped ZnO NPs was studied as follows. In a typical experiment, 0.5 g/L of powder (different Er dopant percentage from 0% to 5%) was immersed in a beaker filled with 500 mL of RR180 aqueous solution with an initial concentration of 50 mg/L. Prior to light irradiation, the solution is left in the dark for 30 min under magnetic agitation until an adsorption–desorption equilibrium is finally established. Thereafter, the assembly was exposed to UV irradiation.

Fig. 7 represents the degradation efficiency of RR180 undoped ZnO and erbium-doped ZnO catalysts as a

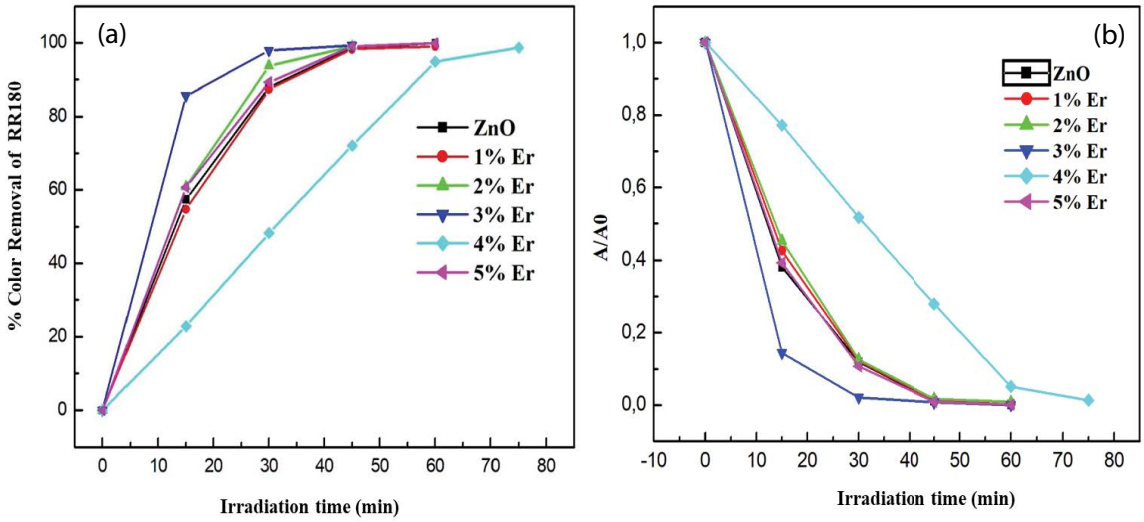

Fig. 7. (a) Photocatalytic color removal rates of the doped ZnO and (b) comparison of photocatalytic degradation of RR180 for different photocatalytic systems as a function of irradiation time under UV light.

function of time. The maximum degradation efficiency of 99% was achieved by using a 3% Er-doped ZnO catalyst within 45 min. As it is shown in the figure, the erbium improves the photocatalytic activity of ZnO. Beyond 3%, the photocatalytic activity of doped ZnO decreases and becomes even lower than that of undoped ZnO. Therefore, a precise amount of dopant could be critical for getting high photocatalytic activity [69].

A similar result has been found in the literature: Divya and Pradyumnan [32] used Er-doped ZnO for degradation of methylene blue (MB) under UV light irradiation and found a maximum of degradation at 0.6% Er. Sin et al. [30] synthesized via a surfactant-free chemical solution route erbium-doped spherical-like ZnO hierarchical nanostructures for degradation of phenol in water under visible light irradiation. Lee et al. [29] reported the effective photodegradation of tartaric acid in water using Er-ZnO microrods photocatalyst under visible light irradiation. When the data are illustrated as time-dependent normalized dye concentration logarithms; linear plots are observed (Fig. 8a) and their equation is expressed by [70]:

$$\ln\left(\frac{A_0}{A}\right) = k \times t \tag{5}$$

where A_0 is the initial absorbance, A is the absorbance at time t and k is the kinetic rate constant.

This means that the decomposition assumes the first-order kinetics; the constant k which is actually the slopes of the lines obtained are measured and seen in Fig. 8b. Thus according to the kinetic study, in the absence of ZnO photocatalysis, a low kinetic rate constant of 0.7515 min^{-1} is calculated for RR180 dye.

It is often noted that even the low concentration of Er doping improves the photocatalytic activity by providing greater k value in comparison with undoped ZnO and the most important one will be that reported for the lowest Er concentration. These values are comparable with those reported for ZnO doped with Sm where the measurements were carried out under the same conditions [29].

On the basis of these experimental tests and earlier studies [32], a possible mechanism for the degradation of dye over doped ZnO NPs has been seen in Fig. 9. The degradation process of dyes with ZnO irradiation can be interpreted in this way. As the photons of energy equal or exceed the distance between prepared ZnO NPs are absorbed, the electron can be transferred to the conductor band from the valence band leaving a vacant or "hole" electron. In general, due to the recombination of electron and hole pairs, the photocatalytic degradations of dyes with bare ZnO were less than doped products. The improved photocatalytic activity of the doped ZnO NPs is not only related to the fact that doping would enhance the absorption capacity of the NPs in solar light, as well as to the suppression of the recombination rate of the e^-/h^+ pairs by trapping the electron, that strengthened the separation of the conduction band. In addition, the higher separation of charges carried by doped ZnO NPs was verified by PL spectra. At the same time, the hole produced in the valence band (h_{VB}^+) can interact with a surface-bound H_2O to produce a highly reactive hydroxyl radical. The degradation of the dyes is caused by superoxide radical anions ($^\bullet O_2^-$) and hydroxyl radicals ($^\bullet OH$) formed under UV light irradiation.

The reason for the high photocatalytic activity of Er-doped ZnO could be explained by the following mechanism. The photocatalytic degradation of dye is initiated by the photoexcitation of the semiconductor, followed by the formation of electron–hole pairs (Eq. (6)). The high oxidative potential of the hole (h_{VB}^+) in the catalyst permits the direct oxidation of the dye (RR180) to reactive intermediates (Eq. (7)) [70].

$$ZnO + h\nu \rightarrow ZnO\ (e_{CB}^- + h_{VB}^+) \tag{6}$$

$$h_{VB}^+ + \text{dye} \rightarrow \text{reactive intermediate} \tag{7}$$

Another reactive intermediate is $OH^\bullet$ which is responsible for the degradation (it is either formed by the decomposition of water (Eq. (8)) or by the reaction of the hole with OH^- (Eq. (9))). The hydroxyl radical and photogenerated

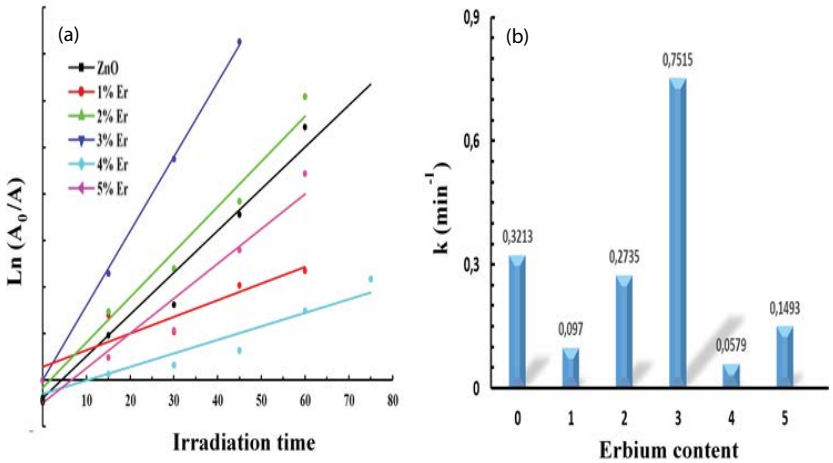

Fig. 8. Photodegradation kinetics of RR180 in the absence and in the presence of ZnO photocatalysts (a) and variation of kinetic constant with Er content (b).

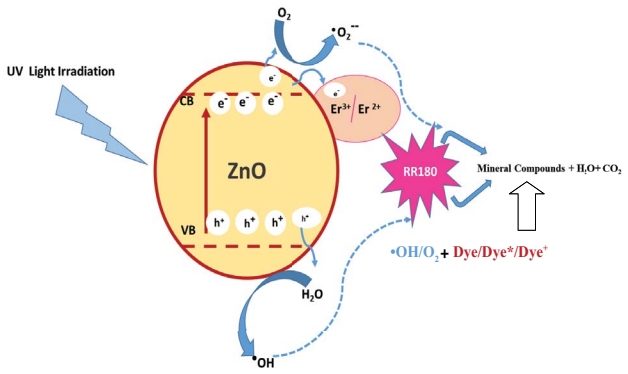

Fig. 9. A plausible mechanism for the degradation of dye using doped ZnO under UV light irradiation.

holes are extremely strong, non-selective oxidants, which induce the partial or complete degradation of several organic chemicals on the catalyst's surface [71].

$$h^+_{VB} + H_2O \rightarrow H^+ + {}^\bullet OH \quad (8)$$

$$h^+_{VB} + OH^- \rightarrow {}^\bullet OH \quad (9)$$

$$Er^{3+} + O_2 \rightarrow Er^{2+} + O_2 \quad (10)$$

$$e^+_{CB} + O_2 \rightarrow {}^\bullet O_2^- \quad (11)$$

$${}^\bullet O_2^- + \text{dye} \rightarrow \text{dye} - OO^\bullet \quad (12)$$

$${}^\bullet O_2^- + HO_2^\bullet + H^+ \rightarrow H_2O_2 + O_2 \quad (13)$$

Electron in the conduction band (e^-_{CB}) can reduce molecular oxygen to superoxide anion (Eq. (11)). This radical, in the presence of organic scavengers, may form organic peroxides (Eq. (12)) or hydrogen peroxide (Eq. (13)). The hydroxyl radical that acts as a strong oxidizing agent that degrades dye into mineral acid and CO_2:

$$\frac{{}^\bullet OH}{{}^\bullet O_2^-} + \text{dye} \rightarrow \text{degradation of the dye} \quad (14)$$

Under the irradiation, erbium ions work as an electronic scavenger, which may act with the superoxide species and limit the electron–hole pair recombination, and thus increases photocatalytic activity [72–74].

When the concentration of erbium is increased further, the activity of the catalyst for the degradation of RR180 decreases. It is interesting to note that the intensity of deep level emission in the PL spectrum is maxima also at 3%, which mentions that the two properties are linked. A similar result was reported in the case of neodymium-doped ZnO used for the degradation of C.I. Reactive Blue 4 [39].

On the other hand, the main reason for the decrease of photocatalytic activity of a wide band gap semiconductor is the recombination of electron–hole pairs in the redox processes [32,71–73]. Erbium doping results in the production of interstitial oxygen Oi and anti-site oxygen O_{Zn}, which play a very important role in the trapping of charge carriers by preventing them from recombination. Doping of trivalent impurity such as erbium in ZnO will result in the creation of more and more electrons and a hole, which also serves to improve photocatalytic activity.

The decrease in the crystallite size with doping can be considered as another reason for the enhancement of photocatalytic activity. Decreasing the average particle size increases the number of surface sites available for charge transfer. Moreover, decreasing the particle size also increases the rate of surface charge recombination. Therefore, the formation of the rate of electron–hole pairs on the catalyst surface will increase greatly which resulted in higher photocatalytic efficiency. For a sufficiently small particle size, surface recombination becomes the dominant process as the charge carriers are formed close to the particle surface and because the recombination process is faster than interfacial charge transfer is at 3 wt.% erbium doping. The crystallite size is reduced to a minimum compared with other samples (evident from SEM results) indicating the maximum surface area of the sample, resulting in maximum photocatalytic activity.

4. Conclusion

The structural, morphological and optical properties of erbium-doped ZnO synthesized via a simple solid-state reaction route were investigated. Since rare earth elements have larger ionic radii compared with zinc, the incorporation of trivalent Er ions into ZnO host lattice can cause a significant distortion in the ZnO crystal lattice. The incorporation of Er in ZnO was confirmed using EDS analysis. The crystallite size calculated using the Debye Scherrer formula and is found to be decreased with doping up to the optimal concentration of 3 wt.% Er. According to the SEM images, a large irregular shaped morphology of pure ZnO is changed to nanosized spherical at the optimum doping concentration. Samples show weak emission in the UV region and an enhanced emission in the visible region after erbium doping. Induced defects such as O_{Zn} anti-site oxygen and interstitial oxygen Oi, due to Er doping at optimal mass ratio 3 wt.%, could be responsible for the increase in visible emission. The photocatalytic activity of ZnO in terms of color removal is enhanced with erbium doping at 3 wt.% concentration. The degradation of 99% of RR180 textile dye using 3 wt.% Er was obtained at 45 min. In addition, the PL presents a maximum emission for ZnO doped with 3% of erbium as it is the case of the photocatalytic activity. Both photocatalytic activity and photoluminescence properties of ZnO show their maximum at 3 wt.% erbium doping.

References

[1] K. Yu, J. Shi, Z. Zhang, Y. Liang, W. Liu, Synthesis, characterization, and photocatalysis of ZnO and Er-Doped ZnO, J. Nanomater., 2013 (2013) 1–5, doi: 10.1155/2013/372951.
[2] A. Akbari, S. Desclaux, J.C. Remigy, P. Aptel, Treatment of textile dye effluents using a new photografted nanofiltration membrane, Desalination, 149 (2002) 101–107.
[3] G. Ciardelli, L. Corsi, M. Marucci, Membrane separation for wastewater reuse in the textile industry, Resour. Conserv. Recycl., 31 (2000) 189–197.

[4] A. Bhatnagar, M. Sillanpaa, Utilization of agro-industrial and municipal waste materials as potential adsorbents for water treatment: a review, Chem. Eng. J., 157 (2010) 277–296.
[5] P. Chandran, P. Kumari, S. Sudheer Khan, Photocatalytic activation of CdS NPs under visible light for environmental cleanup and disinfection, Sol. Energy, 105 (2014) 542–547.
[6] N. Kislov, J. Lahiri, H. Verma, D.Y. Goswami, E. Stefanakos, M. Batzill, Photocatalytic degradation of methyl orange over single crystalline ZnO: orientation dependence of photoactivity and photostability of ZnO, Langmuir, 25 (2009) 3310–3315.
[7] G. Yanga, Z. Yanb, T. Xiao, Preparation and characterization of SnO_2/ZnO/TiO_2 composite semiconductor with enhanced photocatalytic activity, Appl. Surf. Sci., 258 (2012) 8704–8712.
[8] A. Hamrouni, N. Moussa, F. Parrino, A.D. Paola, A. Houas, L. Palmisano, Sol-gel synthesis and photocatalytic activity of ZnO-SnO_2 nanocomposites, Mol. Catal. A, 390 (2014) 133–141.
[9] H. Chemingui, T. Missaoui, J. Chékir Mzali, T. Yildiz, M. Konyar, M. Smiri, N. Saidi, A. Hafiane, H.C. Yatmaz, Facile green synthesis of zinc oxide nanoparticles (ZnO NPs): antibacterial and photocatalytic activities, Mater. Res. Express, 6 (2019) 1050b4.
[10] J. Cui, U. Gibson, Low-temperature fabrication of single-crystal ZnO nanopillar photonic bandgap structures, Nanotechnology, 18 (2007) 155302.
[11] S. Chakrabarti, B.K. Dutta, Photocatalytic degradation of model textile dyes in wastewater using ZnO as semiconductor catalyst, J. Hazard. Mater., 112 (2004) 269–278.
[12] A.B. Djurisic, X.Y. Chen, Y.H. Leung, A.M.C. Ng, ZnO nanostructures: growth, properties and applications, J. Mater. Chem., 22 (2012) 6526–6535.
[13] A. Elkhidir Suliman, Y. Tang, L. Xu, Preparation of ZnO nanoparticles and nanosheets and their application to dye-sensitized solar cells, Sol. Energy Mater. Sol. Cells, 91 (2007) 1658–1662.
[14] K. Tang, S.L. Gu, S.Z. Li, J.D. Ye, S.M. Zhu, H. Chen, Temperature-dependent photoluminescence of ZnO films codoped with tellurium and nitrogen, J. Vac. Sci. Technol., A, 29 (2011) 1–7.
[15] N. Bouhssira, S. Abed, E. Tomasella, J. Cellier, A. Mosbah, M.S. Aida, M. Jacquet, Influence of annealing temperature on the properties of ZnO thin films deposited by thermal evaporation, Appl. Surf. Sci., 252 (2006) 5594–5597.
[16] S. Jurablu, M. Farahmandjou, T.P. Firoozabadi, Sol-gel synthesis of zinc oxide (ZnO) nanoparticles: study of structural and optical properties, J. Sci. Islamic Republic of Iran, 26 (2015) 281–285.
[17] H. Chemingui, M. Smiri, T. Missaoui, A. Hafiane, Zinc oxide nanoparticles induced oxidative stress and changes in the photosynthetic apparatus in fenugreek (*Trigonella foenum-graecum* L.), Bull. Environ. Contam. Toxicol., 102 (2019) 326.
[18] X. Qiu, G. Li, X. Sun, L. Li, X. Fu, Doping effects of Co^{2+} ions on ZnO nanorods and their photocatalytic properties, Nanotechnology, 19 (2008) 215–703.
[19] M. Sharrouf, R. Awad, S. Marhaba, D. El-Said Bakeer, Structural, optical and room temperature magnetic study of Mn doped ZnO nanoparticles, NANO: Brief Rep. Rev., 11 (2016) 1650042.
[20] N, Aisah, D. Gustiono, V. Fauzia, I. Sugihartono, R. Nuryadi, Synthesis and enhanced photocatalytic activity of Ce-doped zinc oxide nanorods by hydrothermal method, Mater. Sci. Eng., 172 (2017) 012037.
[21] P.V. Korake, A.N. Kadam, K.M. Garadkar, Photocatalytic activity of Eu^{3+}-doped ZnO nanorods synthesized via microwave assisted technique, J. Rare Earths, 32 (2014) 306–313.
[22] M. Rezaei, A. Habibi-Yangjeh, Microwave-assisted preparation of Ce-doped ZnO nanostructures as an efficient photocatalyst, Mater. Lett., 110 (2013) 53–56.
[23] M. Faisal, A.A. Ismail, A.A. Ibrahim, H. Bouzid, S.A. Al-Sayari, Highly efficient photocatalyst based on Ce doped ZnO nanorods: controllable synthesis and enhanced photocatalytic activity, Chem. Eng. J., 229 (2013) 225–233.
[24] S. Gao, H. Zhang, R. Deng, X. Wang, D. Sun, G. Zheng, Ballisticity of nanotube field-effect transistors: role of phonon energy and gate bias, Appl. Phys. Lett., 89 (2006) 23125–23128.
[25] N. Mais, J.P. Reithmaier, A. Forchel, M. Kohls, L. Spanhel, G. Muller, Er doped nanocrystalline ZnO planar waveguide structures for1.55 μm amplifier applications, J. Appl. Phys. Lett., 75 (1999) 2005–2008.
[26] A. Polman, Erbium implanted thin film photonic materials, J. Appl. Phys., 82 (1997) 1–39.
[27] K. Takahei, A. Taguchi, Selective formation of an efficient Er–O luminescence center in GaAs by metal organic chemical vapor deposition under an atmosphere containing oxygen, J. Appl. Phys., 74 (1993) 1979–1983.
[28] R. Zamiri, A. Kaushal, A. Rebelo, J.M.F. Ferreira, Er doped ZnO nanoplates: synthesis, optical and dielectric properties, Ceram. Int., 40 (2014) 1635–1639.
[29] G.J. Lee, Ch.Y. Lin, J.J. Wu, Preparation of Dumbbell-like Er/ZnO Microrods with efficient energy upconversion for the catalytic degradation of tartaric acid in water, Topics Catal., 60 (2017)1359.
[30] J.Ch. Sin, S.M. Lam, K.T. Lee, Abd. R. Mohamed, Fabrication of erbium-doped spherical-like ZnO hierarchical nanostructures with enhanced visible light-driven photocatalytic activity, Mater. Lett., 91 (2013) 1–4.
[31] A. Khataee, S. Saadi, M. Safarpour, S.W. Joo, Sonocatalytic performance of Er-doped ZnO for degradation of a textile dye, Ultrason. Sonochem., 27 (2015) 379–388.
[32] N.K. Divya, P.P. Pradyumnan, Solid state synthesis of erbium doped ZnO with excellent photocatalytic activity and enhanced visible light emission, Mater. Sci. Semicond. Process., 41 (2016) 428–435.
[33] W. Raza, S.M. Faisal, M. Owais, D. Bahnemann, M. Muneer, Facile fabrication of highly efficient modified ZnO photocatalyst with enhanced photocatalytic, antibacterial and anticancer activity, RSC Adv., 6 (2016) 78335.
[34] A. Kocakusakoglu, M. Daglar, M. Konyar, H.C. Yatmaz, K. Öztürk, Photocatalytic activity of reticulated ZnO porous ceramics in degradation of azo dye molecules, J. Eur. Cerm. Soc., 35 (2015) 2845–2853.
[35] P. Klug, L.E. Alexander, X-Ray Diffraction Procedures: For Polycrystalline and Amorphous Materials, 2nd ed., Wiley, New York, 1954.
[36] R. John, R. Rajakumari, Synthesis and characterization of rare Earth ion doped nano ZnO, Nano-Micro Lett., 4 (2012) 65–72.
[37] A. Guesmi, C. Bouzidi, H. Elhouichet, Spectroscopic properties of Dy^{3+} doped ZnO for white luminescence applications, Spectrochim. Acta Part A, 177 (2017) 164–169.
[38] Y. Zhou, S.X. Lu, W.G. Xu, Photocatalytic activity of Nd-doped ZnO for the degradation of C.I. Reactive Blue 4 in aqueous suspension, Environ. Prog. Sustainable Energy, 28 (2009) 226–233.
[39] J.-C. Sin, Sze-Mun Lam, Ichikawa Satoshi, Keat-Teong Lee, A.R. Mohamed, Sunlight photocatalytic activity enhancement and mechanism of novel europium-doped ZnO hierarchical micro/nanospheres for degradation of phenol, Appl. Catal. B, 148–149 (2014) 258–268.
[40] S. Anandan, A. Vinu, T. Mori, N. Gokulakrishnan, P. Srinivasu, V. Murugesan, K. Ariga, Photocatalytic degradation of 2,4,6-trichlorophenol using lanthanum doped ZnO in aqueous suspension, Catal. Commun., 8 (2007) 1377–1382.
[41] D. Suresh, P.C. Nethravathi, Udayabhanu, M.A. PavanKumar, H. Raja Naika, H. Nagabhushana, S.C. Sharma, Chironji mediated facile green synthesis of ZnO nanoparticles and their photoluminescence, photodegradative, antimicrobial and antioxidant activities, Mater. Sci. Semicond. Process., 40 (2015) 759–765.
[42] B. El Filali, T.V. Torchynska, A.I. Diaz Cano, Defect related emission of ZnO and ZnO Cu nanocrystals prepared by electrochemical method, J. Lumin., 161 (2015) 25–30.
[43] A. Jagannatha Reddy, M.K. Kokila, H. Nagabhushana, J.L. Rao, C. Shivakumara, B.M. Nagabh ushana, R.P.S. Chakradhar, Combustion synthesis, characterization and Raman studies of ZnO nanopowders, Spectrochim. Acta A, 81 (2011) 53–58.
[44] S. Arunkumar, K. Marimuthu, Concentration effect of Sm^{3+} ions in B_2O_3–PbO–PbF_2–Bi_2O_3–ZnO glasses–structural and

luminescence investigations, J. Alloys Compd., 565 (2013) 104–114.
[45] N.A. Salahuddin, M. El-Kemary, E.M. Ibrahim, Synthesis and characterization of ZnO nanoparticles via precipitation method: effect of annealing temperature on particle size, Nanosci. Nanotechnol., 5 (2015) 82–88.
[46] G.A. Suganya Josephine, A. Sivasamy, Nanocrystalline ZnO doped Dy_2O_3 a highly active visible photocatalyst: the role of characteristic f orbital's of lanthanides for visible photoactivity, Appl. Catal. B, 150 (2014) 288.
[47] S.-m. Chang, R.-a. Doong, The effect of chemical states of dopants on the microstructures and band gaps of metal-doped ZrO_2 thin films at different temperatures, J. Phys. Chem. B, 108 (2004) 18098–18103.
[48] S. Zhang, Y. Chen, Y. Yu, H, Wu, S. Wang, B. Zhu, W. Huang, S. Wu, Synthesis, characterization of Cr-doped TiO_2 nanotubes with high photocatalytic activity, J. Nanopart. Res., 10 (2008) 871–875.
[49] M. Faraz, F.K. Naqvi, M. Shakir, N. Khare, Synthesis of samarium-doped zinc oxide nanoparticles with improved photocatalytic performance and recyclability under visible light irradiation, New J. Chem., 42 (2018) 2295–2305.
[50] P.V. Korake, A.N. Kadam, K.M. Garadka, Photocatalytic activity of Eu^{3+}-doped ZnO nanorods synthesized via microwave assisted technique, J. Rare Earths, 32 (2014) 306–313.
[51] R.Y. Hong, J.H. Li, L.L. Chen, D.Q. Liu, H.Z. Li, Y. Zheng, J. Ding, Synthesis, surface modification and photocatalytic property of ZnO nanoparticles, Powder Technol., 189 (2009) 426–432.
[52] A. Jagannatha Reddy, M.K. Kokila, H. Nagabhushana, J.L. Rao, C. Shivakumara, B.M. Nagabhushana, R.P.S. Chakradhar, Spectrochim. Acta A, 81 (2011) 53–58.
[53] J. Lang, J. Wang, Q. Zhang, S. Xu, D. Han, J. Yang, Q. Han, L. Yang, Y. Sui, X. Li, X. Liu, Structural, optical and EPR studies on ZnO:Cu nanopowders prepared via low temperature solution combustion synthesis, Mater. Sci. Semicond. Process., 41 (2016) 32–37.
[54] W. Bousslama, H. Elhouichet, B. Gelloz, B. Sieber, A. Addad, M. Moreau, M. Férid, N. Koshida, Structural and luminescence properties of highly crystalline ZnO nanoparticles prepared by sol–gel method, Jpn. J. Appl. Phys., 51 (2012) 04–13.
[55] A. Joseph, G.L Praveen, K. Abha, G.M. Lekha, S. George, Photoluminescence study on amino functionalized dysprosium oxide–zinc oxide composite bifunctional nanoparticles, J. Lumin., 132 (2012) 1999–2004.
[56] N. Karak, B. Pal, D. Sarkar, T. Kumar Kundu, Growth of Co-doped ZnO nanoparticles by porous alumina assisted sol–gel route: structural optical and magnetic properties, J. Alloys Compd., 647 (2015) 252–258.
[57] F. Empizo Melvin John, K. Fukuda, R. Arita, Y. Minami, K. Yamanoi, T. Shimizu, N. Sarukura, M. Vargas Ray, A. Salvador Arnel, V. Sarmago Roland, Photoluminescence properties of a single ZnO microstructure for potential scintillator applications, Opt. Mater., 38 (2014) 256–260.
[58] A. Kovalenko, G. Pourroy, O. Crégut, M. Gallart, B. Hönerlage, P. Gilliot, Evidence of unintentional *n*-doping in ZnO nanorods, J. Phys. Chem. C, 114 (2010) 9498–9502.
[59] M. Navaneethan, J. Archana, M. Arivanandhan, Y. Hayakawa, Functional properties of amine-passivated ZnO nanostructures and dye-sensitized solar cell characteristics, Chem. Eng. J., 213 (2012) 70–77.
[60] M. Navaneethan, J. Archana, M. Arivanandhan, Y. Hayakawa, Chemical synthesis of ZnO hexagonal thin nanodisks and dye-sensitized solar cell performance, Phys. Status Solidi RRL, 6 (2012) 120–122.
[61] L.-L. Yang, J.-H. Yang, D.-D. Wang, Y.-J. Zhang, Ya-Xin Wang, Hui-Lian Liu, Hou-Gang Fan, Ji-Hui Lang, Photoluminescence and Raman analysis of ZnO nanowires deposited on Si (1 0 0) via vapor–liquid–solid process, Physica E, 40 (2008) 920–923.
[62] A. Van Dijken, E.A. Meulenkamp, D. Vanmaekelbergh, A. Meijerink, The kinetics of the radiative and nonradiative processes in nanocrystalline ZnO particles upon photoexcitation, J. Phys. Chem. B, 104 (2000) 1715–1723.
[63] D. Sarkar, S. Tikku, V. Thapar, R.S. Srinivasa, K.C. Khilar, Formation of zinc oxide nanoparticles of different shapes in water-in-oil microemulsion, Colloids Surf. A, 381 (2011) 123–129.
[64] K. Vanheusden, C.H. Seager, W.L. Warren, D.R. Tallant, J.A. Voigt, Correlation between photoluminescence and oxygen vacancies in ZnO phosphors, Appl. Phys. Lett., 68 (1996) 403–407.
[65] P.K. Sanoop, S. Anas, S. Ananthakumar, V. Gunasekar, R. Saravanan, V. Ponnusami, Synthesis of yttrium doped nanocrystalline ZnO and its photocatalytic activity in methylene blue degradation, Arabian J. Chem., 9 (2016) S1618–S1626.
[66] Z. Zhao, J.-l. Son, G.-h. Zhen, G.J.-s. Lian, Optical properties and photocatalytic activity of Nd-doped ZnO powders, Trans. Nonferrous Met. Soc. China, 24 (2014) 1434–1439.
[67] I. Jlassi, H. Elhouichet, M. Ferid, R. Chtourou, M. Oueslati, Study of photoluminescence quenching in Er^{3+}-doped tellurite glasses, Opt. Mater., 32 (2010) 743–747.
[68] R.S. Ajimsha, A.K. Das, B.N. Singh, P. Misra, L.M. Kukreja, Structural, electrical and optical properties of Dy doped ZnO thin films grown by buffer assisted pulsed laser deposition, Physica E, 42 (2010) 1838–1843.
[69] J. Zhang, S.J. Deng, S.Y. Liu, J.M. Chen, B.Q. Han, Y. Wang, Y.D. Wang, Preparation and photocatalytic activity of Nd doped ZnO nanoparticles, J. Mater. Technol., 29 (2013) 263–267.
[70] M.A. Behnajady, N. Modirshahla, R. Hamzavi, Kinetic study on photocatalytic degradation of C.I. Acid Yellow 23 by ZnO photocatalyst, J. Hazard. Mater. B, 133 (2006) 226–232.
[71] N. Daneshvar, D. Salari, A. Khataee, Photocatalytic degradation of azo dye acid red 14 in water: investigation of the effect of operational parameters, J. Photochem. Photobiol. A, 157 (2003) 111–128.
[72] A. Khataee, R. Darvishi, Ch. Soltani, Y. Hanifehpour, M. Safarpour, H.G. Ranjbar, S.W. Joo, Synthesis and characterization of dysprosium doped ZnO nanoparticles for photocatalysis of a textile dye under visible light irradiation, Ind. Eng. Chem. Res., 53 (2014) 1924–1932.
[73] A. Khataee, Y. Hanifehpour, M. Safarpour, M. Hosseini, S. Joo, Synthesis and characterization of $Er_xZn_{(1-x)}Se$ nanoparticles: a novel visible light responsive photocatalyst, Sci. Adv. Mater., 5 (2013) 1074–1082.
[74] M. Khatamian, B. Divband, A. Jodaei, Degradation of 4-Nitrophenol (4-NP) using ZnO nanoparticles supported on zeolites and modeling of experimental results by artificial neutral networks, Mater. Chem. Phys., 134 (2012) 31.